ORIGINAL ARTICLE

Prediction of cross-sectional features of SPR joints based on the punch force-displacement curve using machine learning

Borja Ferrándiz[1,2] · Monzer Daoud[3] · Nicolas Kohout[2] · Francisco Chinesta[1]

Abstract

Self-piercing riveting has gained relevance in the automotive industry as an alternative method to resistance spot welding for the joining of two or more metal sheets. Its simulation via the finite element method, which includes large deformation, plasticity, and fracture mechanics phenomena, has been previously studied in depth. However, costly experimental tests are still required for the characterization of several uncertain variables such as the mechanical properties of all materials, or the friction coefficients of all existing contact pairs. This paper proposes a machine learning model, which can be trained with both experimental and numerical data, in order to predict the cross-sectional features of the riveted joint from the corresponding punch force-displacement curves, such as the interlock distance or the minimum thickness of the lower sheet. In order to achieve this goal, a parametric study has been first carried out by means of a finite element model, by varying the mechanical properties of the upper and lower sheet materials as well as the friction coefficients, while keeping constant the rivet material and all geometries involved. All the obtained force-displacement curves, defined by a large number of points, have been initially projected to a lower-dimensional space via a convolutional autoencoder. Then, a multilayer perceptron has been used to associate their latent space to their corresponding final geometric features. It was found that there is a strong correlation between the force-displacement curves and the final geometric features, allowing for further studies including variation in the geometry or in the rivet material.

Keywords SPR · Self-piercing riveting · Machine learning · Model order reduction · Autoencoder

1 Introduction

Self-piercing riveting (SPR) is a high-speed cold mechanical fastening technique suitable for point-joining two or more metal sheets. SPR has become a widely used technique in the automobile industry, due to the increasing use of new lightweight materials (such as aluminum) and alloys, or even dissimilar material combinations that are difficult or impossible to weld [1, 2].

This metal forming process creates a strong mechanical interlock by driving downwards a hollow tubular rivet, under the effect of a hydraulic punch, piercing through the upper sheet or the upper and middle sheets and flaring outwards in the bottom sheet under the guidance of the die geometry (see Fig. 1).

In addition to SPR, there are other joining technologies available. Resistance spot welding (RSW) [3] and clinching [4–7] are examples of alternative methods that often offer lower costs per joint than SPR. However, it has been found that SPR exhibits superior behavior to RSW and clinching under tensile and shear static or fatigue loadings [2, 8–11].

The quality of the SPR joint can be determined by means of some cross-sectional features, e.g., interlock distance or minimum thickness of the lower sheet (shown in Fig. 1b), which in turn are affected by the process variables: the rivet and die geometries, thicknesses of the upper and lower sheets, employed materials, punch speed, and friction phenomena, to name a few. For instance, it was shown in [1] that for a given set of rivet/die geometries as well as the choice of

✉ Borja Ferrándiz
borja.ferrandiz@ensam.eu

[1] PIMM Laboratory, Arts et Métiers Institute of Technology, 151 boulevard de l'Hôpital, 75013 Paris, France

[2] French Technological Research Institute for Materials, Metallurgy and Processes (IRT- M2P), 4 rue Augustin Fresnel, 57070 Metz, France

[3] Department of Mechanical and Mechatronics Engineering, College of Engineering, Dhofar University, Salalah 211, Oman

Fig. 1 Schematic of the SPR process

(a) Initial arrangement.   (b) Punch descent and perforation.
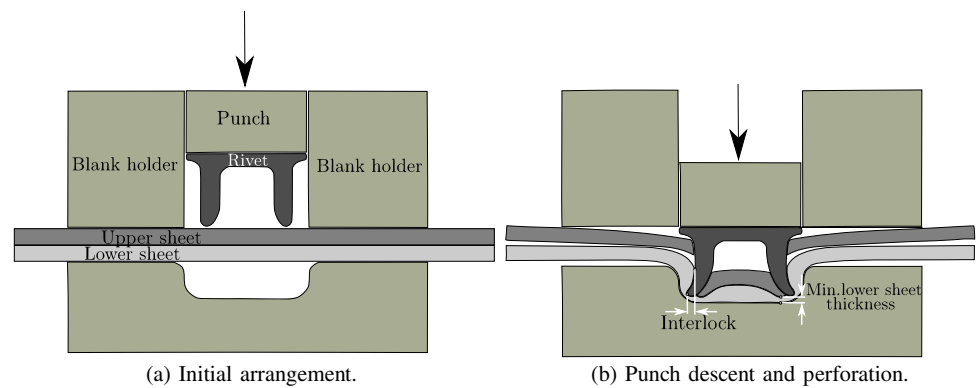
materials, only certain combinations of thicknesses of the upper and lower sheets (t_u and t_l, respectively) will produce a successful SPR joint.

The mechanical behavior of the whole riveted structure can be substantially affected by the quality of the SPR joints. As a result, different approaches were used in the literature to determine the quality of the riveted connection.

Several studies involving experimental SPR tests [12–16] can be found in the literature, which focus mainly on the analysis of the final geometry, microstructure and punch force-displacement curves, and their dependence on process variables such as the maximum attainable punch load. However, this experimental approach is costly and time consuming. In fact, in the case of a new configuration (new materials, new rivet/die combination, change in the thickness of joined sheets, etc.), the automotive industry has to carry out experimental tests to check the feasibility and strength of the riveted connection in order to ensure that the latter meets the technical specifications.

The most attractive computational tool to avoid the experimental trial and error approach is the finite element method (FEM). It has proven to be highly efficient for better understanding the mechanisms involved in the SPR process [17–22]. However one can find in the literature disparate data for characterizing the visco-plastic behavior of the materials under consideration as well as the friction behavior between the corresponding contact pairs. Porcaro et al. [18] developed a comprehensive 2D axisymmetric model for simulating the SPR process using the commercial software LS-Dyna. In this work, the Coulomb friction law and strain-rate-independent hardening coupled with an adaptive remeshing strategy were used. A geometry-based failure criteria was implemented to allow the splitting of the upper sheet during the rivet insertion. Daoud et al. [19] considered the strain-rate-dependent Hansel-Spittel model for plasticity in combination with the Coulomb friction law and a geometric-fracture criterion. In both works, the predicted force-displacement curves were in good agreement with the experimental ones. More recent works [20–22] adopted the element deletion (also called "kill-element") technique along with a material damage

criterion. In this technique, damage D is initially set to 0 for every element and is integrated up to 1 when the element is killed, i.e., removed from the mesh. More concretely, Casalino et al. [22] defined a constant plastic strain at failure ($\varepsilon_p = 1.5$) coupled with a strain-rate-independent empirical plasticity model. The Hosford-Coulomb damage model was introduced in [20] along with the rate-independent Swift-Voce hardening law and an explicit time integration scheme.

Machine learning (ML) algorithms have also been applied to the SPR problem, permitting to bypass the costly and time-consuming aforementioned experimental or numerical approaches in order to evaluate the quality of the joint. The developed ML-based models can be trained using data from experiments and/or simulations during the offline phase. For instance, the multilayer perceptron (MLP) [23] is a simple technique capable of extracting complex nonlinear patterns between the process variables and the corresponding outputs [24]. Zhao et al. [25] used a MLP to predict key geometric features (such as the interlock length) from five process parameters (thicknesses of metal sheets, geometric dimensions of the rivet/die). Karathanasopoulos et al. [20] developed a similar model to predict the feasibility of the SPR under a combination of four variables, producing as output a score between -1 (unfeasible) and +1 (feasible). Meanwhile, Fang et al. [26] implemented a ML scheme to calibrate some uncertain simulation parameters, e.g., friction coefficients for the multiple contact pairs, in order to minimize the discrepancy between a given model and the experimental data. Besides, more intricate studies have been carried out by the use of deep-learning models [27], such as autoencoders [28, 29] and generative adversial networks (GAN) [30]. Oh et al. [31] developed a convolutional autoencoder (CAE) to segment cross-sectional rivet images, and a GAN to create a graphical evolution of the cross section along with the maximum punch force. Likewise, Kim et al. [32] used a GAN that was able of printing the cross section of the SPR joint based on the mechanical properties of both upper and lower sheets (Young's modulus, Poisson's ratio and ultimate tensile strength).

As aforementioned, costly experimental tests have to be carried out to check the feasibility and joint strength every time a new material combination for the sheets is implemented, whereas the numerical analysis involves the tuning of some uncertain parameters such as friction coefficients. Hence, the aim of this work lies in the development of a ML scheme that allows to evaluate the final cross-sectional geometry features from only the punch force-displacement curve, hence avoiding characterization tests. For this purpose, first a finite element (FE) model using the commercial software ABAQUS is implemented in Section 2 and validated in Section 3. The proposed ML model and data sampling method are described in Section 4. Finally, results are presented in Section 5 and the main conclusions are withdrawn in Section 6.

2 Finite element modeling

2.1 Material models and governing equations

There are diverse plasticity and damage models for each of the three considered materials, and their choice has a noticeable influence on the results (force-displacement curve and geometry of the final cross section). Following [19], the von Mises yield criterion [33] was applied in combination with isotropic work hardening to model the behavior of the rivet and sheets. The yield function f, defining the yield surface, is expressed as:

$$f\left(\bar{\sigma}, \bar{\varepsilon}_p\right) = \bar{\sigma} - k\left(\bar{\varepsilon}_p\right) , \tag{1}$$

where $\bar{\sigma}$, k and $\bar{\varepsilon}_p$ are the von Mises equivalent stress, the isotropic hardening parameter, and the equivalent plastic strain, respectively [20]. $\bar{\sigma}$ can be obtained from the deviatoric stress tensor s according to:

$$\bar{\sigma} = \sqrt{\frac{3}{2} s : s} , \tag{2}$$

whereas $\bar{\varepsilon}_p$ can be expressed as:

$$\bar{\varepsilon}_p = \int \sqrt{\frac{2}{3} d\varepsilon_p : d\varepsilon_p} . \tag{3}$$

Isotropic work hardening was described by the Hansel-Spittel (HS) [33] hardening rule. Here, the isotropic hardening parameter is defined as:

$$k\left(\bar{\varepsilon}_p\right) = A e^{m_1 \times T} \left(\bar{\varepsilon}_p\right)^{m_2} e^{\left(\frac{m_4}{\varepsilon_p}\right)} \left(\dot{\bar{\varepsilon}}_p\right)^{m_3} , \tag{4}$$

where $\dot{\bar{\varepsilon}}_p$ and T are the equivalent plastic strain rate and temperature, respectively; and A, m_1, m_2, m_3 and m_4 are material constants. Preliminary results showed that thermal conductivity phenomena of the heat generated by friction and plastic deformation has little influence on the results [15, 20].

On the other hand, the Hosford-Coulomb material failure model [34] is considered throughout this work to allow the splitting of the upper sheet during the rivet insertion. Thus, the plastic strain at failure ε_f^{pr} depends only on the stress triaxiality η (ratio of hydrostatic σ_H to von Mises stress $\bar{\sigma}$) and Lode angle θ (a measure of loading type), which are defined as follows [35]:

$$\eta = \frac{\operatorname{tr}(\boldsymbol{\sigma})/3}{\bar{\sigma}} , \tag{5}$$

$$\cos(3\theta) = \left(\frac{r}{q}\right)^3 , \tag{6}$$

where r and q are respectively the scaled version of the second and third deviatoric stress invariants (J_2 and J_3), defined as [35]:

$$q = \sqrt{3J_2} = \bar{\sigma} , \tag{7}$$

$$r = \left(\frac{27J_3}{2}\right)^{1/3} = \left(\frac{27\det(s)}{2}\right)^{1/3} . \tag{8}$$

Thus, material damage D is evaluated locally (at element level), following the basic evolution equation [20, 34]:

$$d D = \frac{d \bar{\varepsilon}_p}{\varepsilon_f^{pr}\left(\eta, \bar{\theta}\right)} , \tag{9}$$

where the final expression for the plastic strain at failure is then:

$$\varepsilon_f^{pr} = b(1+c)^{\frac{1}{p}} \left(\left\{\frac{1}{2}\left((f_1 - f_2)^a + (f_2 - f_3)^a + (f_1 - f_3)^a\right)\right\}^{\frac{1}{a}} + c(2\eta + f_1 + f_3)\right)^{-\frac{1}{p}}, \tag{10}$$

where a, b and c are material-dependent parameters, and p is set to 0.1 for all materials [20]. Functions f_1, f_2 and f_3 only depend on the normalized version of Lode angle $\bar{\theta} = 1 - (6/\pi)\theta$, and are defined as:

$$f_1 = \frac{2}{3} \cos\left(\frac{\pi}{6}(1 - \bar{\theta})\right) , \tag{11}$$

$$f_2 = \frac{2}{3} \cos\left(\frac{\pi}{6}(3 + \bar{\theta})\right) , \tag{12}$$

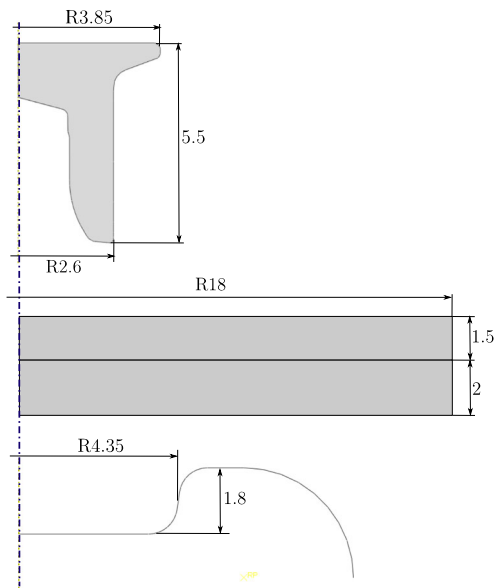$$f_3 = -\frac{2}{3} \cos\left(\frac{\pi}{6}(1 + \bar{\theta})\right) . \tag{13}$$

Fig. 2 Nominal geometries of rivet, sheets and die (dimensions in millimeters)

2.2 Geometries, methods, and implementation

The commercial FE software ABAQUS was used to develop a 2D-axisymmetric FE model of the SPR process. The model is composed of the upper and lower sheets, $\varnothing 5,2 \times 6$-H4 rivet, die (reference M·260·050·21/3-129·F090180), punch, and blank holder, whose geometries, displayed in Fig. 2, were selected according to preliminary feasibility tests [19]. The sheets and rivet, modelled as elastoplastic bodies, were meshed with 4780, 3790, and 1120 isoparametric quadrilateral CAX4R elements, respectively, with 4 integration points, bilinear interpolation, and enhanced hourglass control. Arbitrary Lagrangian Eulerian (ALE) adaptive meshing was used in the lower sheet in order to reduce element distortion. The blank holder and die were considered as analytical rigid bodies.
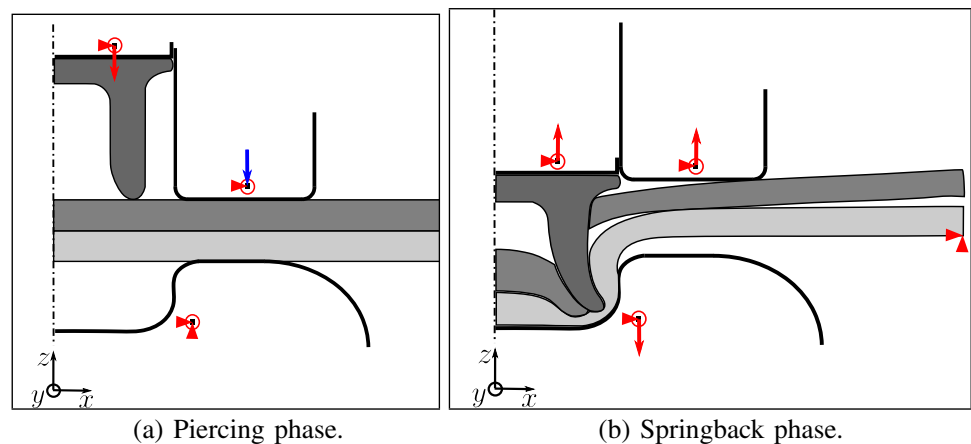
The aforementioned Hansel-Spittel (plasticity) and Swift-Voce (damage) models were introduced in tabular form, and the Coulomb friction law was selected to model the friction of the six contact pairs (see Table 5).

Two different steps were considered during the dynamic analysis (see Fig. 3): (i) the riveting step, during which the punch descends and the rivet pierces the upper sheet and flares outwards; and (ii) the springback step, during which the punch, blank holder, and die are gently retreated. ABAQUS/Explicit is used for the analysis, with double precision and mass scaling (with a target time increment of 1e-7 s).
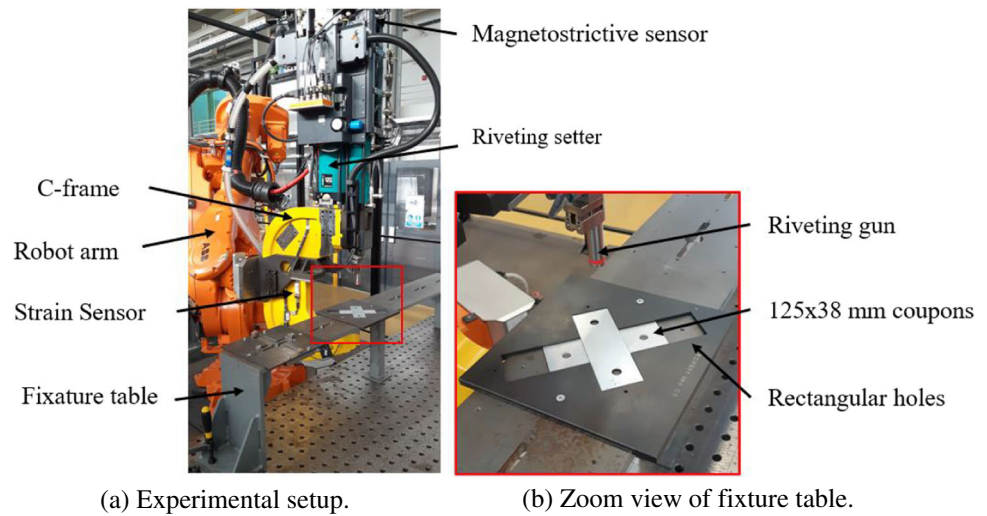
Regarding the boundary conditions, the punch and blank holder are only allowed to move in the vertical direction during the riveting step, i.e., their radial displacement and rotation are constrained. During the first step (i), the punch moves vertically towards the stationary die and punches the rivet against the upper sheet to flare within the lower one under the effect of the die geometry. A downward displacement of 5.3 mm is prescribed to the punch, at a constant speed of 100 mm/s. A downward force of 2.7 kN is meanwhile applied to the blank holder (see Fig. 3a). These values were previously obtained based on a sensitivity study for the setup described in Sections 3 and 5.1 [19].

During the springback phase (ii), the punch, blank holder and die are gently removed, and the displacement of the lower sheet's right bottom node is constrained in the radial and vertical direction to prevent the rigid body motion of the whole (see Fig. 3b).

3 Experimental procedure

The model presented in Section 2.2 has been validated using experimental SPR data [19]. SPR trials were conducted using a pneumo-hydraulic TOX pressotechnik TZ-HSN 08 riveting setter with a maximum riveting force of 80kN, as shown in Fig. 4a. The riveting setter was mounted on a robot arm and positioned near and perpendicular to a fixture table where

Fig. 3 Main steps of SPR process and the kinematic boundary conditions: Constrained radial, vertical displacement (red triangle) and rotation (red circle), prescribed displacement (red arrow) and force (blue arrow)

(a) Piercing phase.

(b) Springback phase.

Fig. 4 SPR trials

(a) Experimental setup.　　(b) Zoom view of fixture table.

several coupons (4 trials) of sizes 38 mm × 125 mm were setup and riveted with a single SPR joint at the center with a rivet head height, describing the position of the rivet head relative to the upper workpiece surface, close to zero as recommended by automotive industry (Renault). All riveting trials were conducted using dissimilar material combinations of the steel DP600 and the aluminum Al5182-O having the nominal thickness of 1.5 mm and 2 mm, respectively, commonly used in automotive applications. As shown in Fig. 4b, coupons are precisely positioned within the fixture table thanks to rectangular holes. The riveting data (force as a function of punch stroke) during the process were recorded using: (1) a strain sensor mounted on the C-frame X-sensor X103-T67-CAL360 (Fig. 4a). The strain measurement is then converted into force via the monitoring system EPW400.

(2) a magnetostrictive sensor Balluff BTL7-A510-M0275 (Fig. 4a) which can measure the stroke with an accuracy up to 10 μm. It is worth mentioning that, by default settings of the setter software, the recorded data are based on the punch stroke increment (10 μm) rather than at a fixed sampling frequency. As far as the cross-sectional features of the riveted joints are concerned, a metallographic preparation was done through 3 steps. First, the riveted joints were cut along the center of the joint. Then, the cross-sectioned samples were cold mounted in epoxy resin and polished, with a final polishing done using a 1 μm colloidal silica. Finally, the macrographs of the samples were performed using a Keyence VHX5000 digital optical microscopy.

It is appropriate to characterize the punch force-stroke curve without C-frame deflection in order to properly
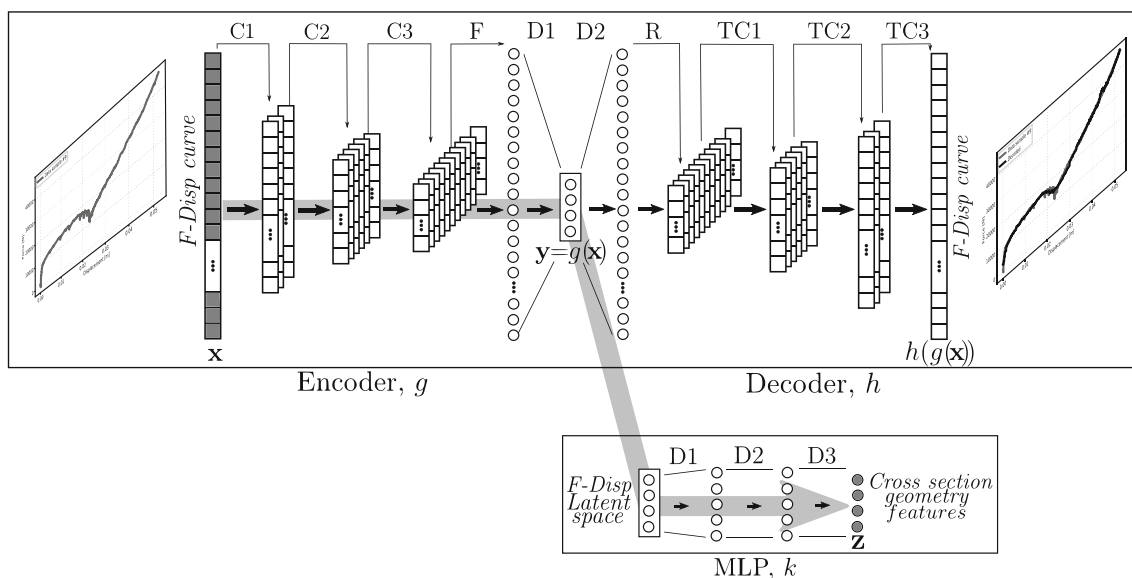

Fig. 5 Machine learning approach: convolutional autoencoder (top) and multilayer perceptron (bottom)

Table 1 Architecture of the encoder with input shape = (875,1). Details concerning convolutional layers: f (number of filters), ks (kernel size), s (stride), p (padding)

Block	Layers	f	ks	s	p	Output
C1	1D Convolution	16	5	5	0	(16,175,1)
	ELU Activation					
C2	1D Convolution	32	5	5	0	(32,35,1)
	ELU Activation					
C3	1D Convolution	64	5	5	0	(64,7,1)
	ELU Activation					
F	Flatten					448
D1	Dense					4
	ELU Activation					

simulate the SPR process. For this purpose, the C-frame deflection was measured by using a flat die as the sole insert and the riveting process was run without any sample or rivet. The displacements were then measured for seven different setting forces: 30, 35, 40, 45, 50, 55, 60 kN. Consequently, force-displacement curves were produced, and an equation representing the C-frame deflection was developed. Finally, by deducing this latter from the one measured during riveting, a corrected punch force-stroke curve was produced, which was compared to the predicted one.

4 Machine learning-based approach

The main goal of this work is to estimate the cross-sectional features **z** of a SPR joint from the force-displacement curve **x**, without necessarily needing to carry out time-consuming experimental characterization tests. For that purpose, a set of (**x**, **z**) tuples obtained numerically has been used to train the

Table 2 Architecture of the decoder. Details concerning convolutions: f (number of filters), ks (kernel size), s (stride), p (padding)

Block	Layers	f	ks	s	p	Output
D2	Dense					448
	ELU Activation					
R	Reshape					(64,7,1)
TC1	1D Transpose convolution	32	5	5	0	(32,35,1)
	ELU Activation					
TC2	1D Transpose convolution	16	5	5	0	(16,175,1)
	ELU Activation					
TC3	1D Transpose convolution	1	5	5	0	(1,875,1)
	Tanh Activation					

Table 3 Layers of the multilayer perceptron (MLP)

Block	Layers	Output
D1	Dense	4
	ELU Activation	
D2	Dense	4
	ELU Activation	
D3	Dense	4
	ELU Activation	

ML model described in Fig. 5 during the offline phase (see Section 4.2 for the materials and friction coefficients sampling).

4.1 ML model

Due to the high number of points defining each force-displacement curve (in this case, 875), a prior dimensionality reduction of this data seems reasonable to extract the most valuable information from them. Then, a nonlinear regression could be constructed in an easier manner between the latent (i.e., reduced) space of the curves and the cross-sectional features (obtained by postprocessing the output *.odb* files). The use of linear dimensionality reduction techniques such as the PCA was found to this aim less efficient than autoencoders in terms of number of modes needed to reconstruct complex functions [36, 37].

Autoencoders are a type of artificial network based on an encoding-decoding structure and capable of nonlinearly reducing dimensionality of unlabeled data from the input size to the latent space's predefined size (located in the middle, see Fig. 5). Among them, convolutional autoencoders have proved to be useful for diverse goals, such as feature extraction of high-dimensional inputs or denoising [38]. They can be decomposed into an encoder (denoted by function g) and a decoder (given by function h). Given an input **x**, the latent space can be denoted by $\mathbf{y} = g(\mathbf{x})$, and the autoencoder output is $h(\mathbf{y}) = h(g(\mathbf{x}))$ [36].
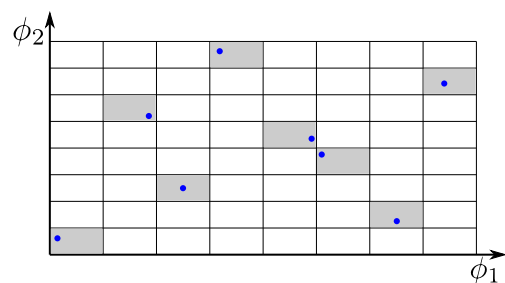

Fig. 6 Latin hypercube sampling (LHS) for a problem of $N = 2$ (variables) and $M = 8$ (sampling size)

Table 4 Ranges for the corresponding mechanical parameters of the upper and lower metal sheets (damage only considered for upper sheet)

	ϕ_i	ϕ_i^{min}	ϕ_i^{max}
Elastic	E [Pa]	60e9	230e9
	ν [Pa]	0.25	0.35
Plastic (Hansel-Spittel)	$Ae^{m_1 \times T}$ [Pa]	200e9	1500e9
	m_2	0.15	0.25
	m_3	0.01	0.03
	m_4	5e-5	5e-4
Damage (Hosford-Coulomb)	a	1	1.5
	b	0.5	1.5
	c	0.05	0.12

Table 5 Friction coefficients for the existent contact pairs

Contact pair	ϕ_i	ϕ_i^{min}	ϕ_i^{max}
Punch – Rivet	μ_1	0.05	0.4
Holder – Upper sheet	μ_2	0.05	0.4
Rivet – Upper sheet	μ_3	0.05	0.4
Rivet – Lower sheet	μ_4	0.05	0.4
Upper sheet – Lower sheet	μ_5	0.05	0.4
Die – Lower sheet	μ_6	0.05	0.4

Thus, the model constructed using PyTorch is illustrated in Fig. 5. It consists of a convolutional autoencoder, which has been first trained with the force-displacement curves **x** provided by ABAQUS software, using a random split ratio of 70:30 for train-test, Adam optimizer, learning rate of 5e-4, and weight decay of 1e-5. The chosen loss function $\mathcal{L}_{CAE}$ is the mean square error (MSE):

$$\mathcal{L}_{CAE} = MSE\left(\mathbf{x}, h\left(g\left(\mathbf{x}\right)\right)\right) . \tag{14}$$

Next, the latent space of each curve has been matched to the corresponding geometric features of interest **z** (interlock distance, minimum lower sheet thickness, center thickness of upper and lower sheets) via an MLP (denoted by function k), which has been trained with a new random test-train split, and the same optimizer parameters as for the CAE. The mean absolute relative error ($MARE$) has been chosen as the loss function:

$$\mathcal{L}_{MLP} = MARE\left(\mathbf{z}, k\left(\mathbf{y}\right)\right) . \tag{15}$$

The architectures of the encoder, decoder and MLP are detailed in Tables 1, 2 and 3, respectively. The choice of the latent space size (of 4) was based on a preliminary iterative test.

4.2 Data sampling

Surrogate models are used to approximate the response of a system without employing time-consuming numerical computations. Thus, an approximate response is obtained from a sparse set of input points within the domain. However, the *a priori* knowledge about the system may be scarce, and the input high dimensionality makes it difficult to design the shape of the sampling. The latin hypercube sampling (LHS) [39] has become increasingly used to generate near-random samples of parameters $\mathbf{\Phi} = \{\phi_1, ..., \phi_N\}$ in high-dimensional problems, achieving great space filling. The range of each of the N variables is cut into M equal-width intervals with the same choice probability, where M is the desired sampling size. Next, random combinations of the intervals are selected, such that each interval is sampled just once. Finally, a point is placed randomly within each of the corresponding associated sub-regions, as shown in Fig. 6.

Regarding the object of this study, the material behavior of the rivet is supposed to be well-known [19], whereas

Fig. 7 Comparison between experimental and predicted SPR force-displacement curves

Fig. 8 Comparison between experimental (image) and predicted (red line) SPR cross section
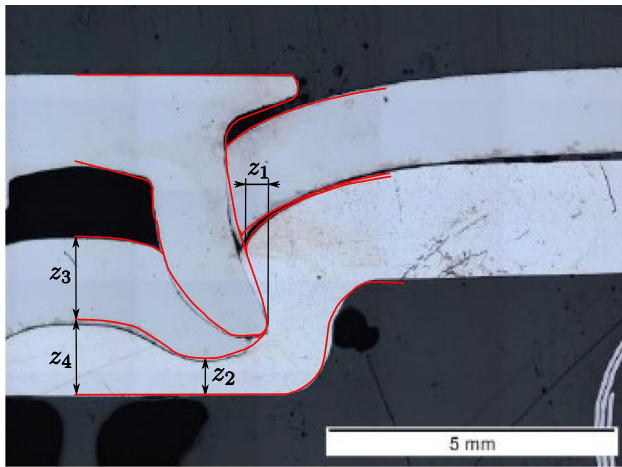
the mechanical behavior of the two riveted sheet metals, are considered as variables. The considered ranges for the elastic, plastic, and damage variables are detailed in Table 4. As mentioned above, the effect of T in Eq. (4) was considered negligible and therefore the term $Ae^{m_1 \times T}$ is considered as one variable for simplicity.

Friction coefficients for the six contact pairs are likewise considered uncertain parameters [26]. The same range of values is regarded for all of them according to Table 5.

Thus, a LHS is produced with $N=21$ variables (material properties and friction coefficients) and $M=400$ data points.

5 Results and discussion

5.1 Validation of the SPR model

Figure 7 shows the experimental curves obtained for the four specimens (see Section 3), as well as the one provided by ABAQUS. A preliminary tuning of the friction coefficients has been carried out to obtain good agreement between both.

Additionally, the final cross section has been pictured and compared with the one obtained numerically (Fig. 8).

In order to give quantitatively a clear comparison, Table 6 shows the values for the geometric features, both obtained experimentally and numerically.

As it can be inferred from Table 6, geometric features are predicted by the ABAQUS model with little error (the greatest relative error is 23.1% for the interlock distance). Authors propose, for example, to introduce a damage model for the lower sheet, with a view to minimizing the discrepancy with the experimental results.

5.2 ML-based prediction of geometry

Results are presented in this section for a latent space dimension of 4. The force-displacement curves (input and output) have been normalized with respect to the maximum admissible riveting force (80 kN). Results will be shown first for the CAE. With only a four-dimensional latent space, $\mathcal{L}_{CAE}$ (MSE) stagnated at 2.78e-4 (for the validation subset) after the training described in Section 4. Figure 9 shows several different simulated force-displacement curves corresponding to the validation dataset, and the decoded curves given by the autoencoder.

As it can be seen in Fig. 9, the CAE is able to efficiently compress the force-displacement curves, while reducing the noise present. Likewise, the four experimental curves obtained in Section 3 are encoded and decoded in a similar fashion, and results are shown in Fig. 10.

Next, the MLP has been trained with simulated data in order to predict key cross-sectional features that allow the assessment of the riveted joint's strength. In this case, all the latent space data (MLP's input) $\mathbf{y}_j$ are standardized $\mathbf{y}_j^{std}$ according to the following expression:

$$y_{i,j}^{std} = \frac{y_{i,j} - \mu_i}{\sigma_i} \, , \tag{16}$$

where subscript $i = \{1, 2, 3, 4\}$ denotes the i-th component of the latent space, j is the sample number in the range $\{1, 400\}$, and μ_i and σ_i denote respectively the mean and standard deviation. Meanwhile, outputs $\mathbf{z}_j$ are standardized following:

$$z_{i,j}^{std} = \frac{z_{i,j} - \mu_i}{\sigma_i} \, , \tag{17}$$

where subscripts $i = \{1, 2, 3, 4\}$ refer to the interlock distance, minimum lower sheet thickness, and center upper and lower sheet thicknesses, respectively. After the training
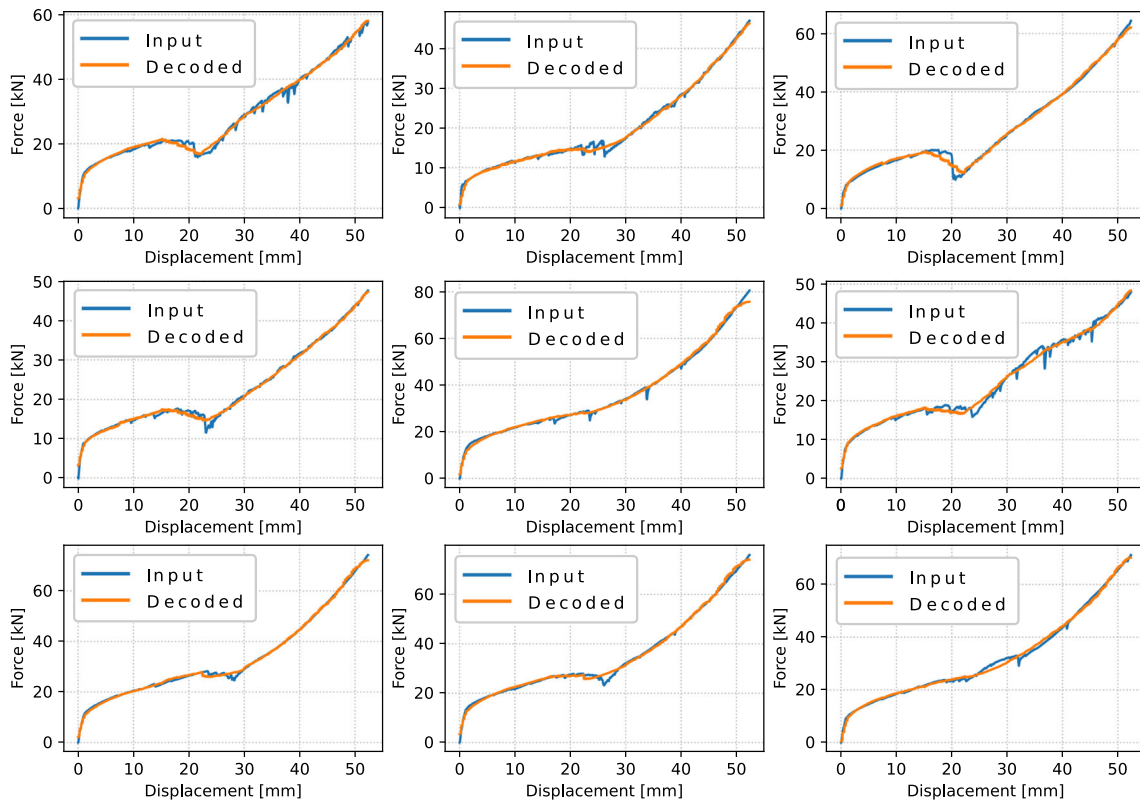
Table 6 Comparison between experimental and predicted SPR cross-sectional features

Cross-sectional feature		Experimental (min - max)	Numerical
Interlock length [mm]	z_1	0.443 - 0.483	0.356
Minimum lower sheet thickness [mm]	z_2	0.528 - 0.634	0.641
Center upper sheet thickness [mm]	z_3	1.482 - 1.529	1.451
Center lower sheet thickness [mm]	z_4	1.218 - 1.257	1.300

Fig. 9 Numerical (ABAQUS) force-displacement curves (input to CAE) and decoded ones (CAE output)

described in Section 4, it has been found that good correlation exists between the curves latent space and the geometric parameters ($MARE$=5.37·10^{-2}). Predictions for the numerical results are shown in Fig. 11, where blue and red dots correspond to the training and validation sets, respectively.

Next, the punch force-displacement curves shown in Fig. 10 have been plugged into the ML model, in order to predict the cross-sectional features, and compare them to the ones obtained experimentally. Note that, while four

experimental force-displacement curves were available, only two riveted specimens were examined using an optical microscope to obtain their geometrical parameters (#2 and #4, represented by the blue and red lines, respectively, in Fig. 12). Additionally, the numerical geometrical parameters obtained by the FE model are represented by the black dashed lines.

It can be seen that the ML predictions based on the experimental curves (blue bars) were generally in good agreement

Fig. 10 Experimental force-displacement curves (solid lines) and corresponding encoded-decoded reconstruction (dashed lines) for specimens #1 – #4
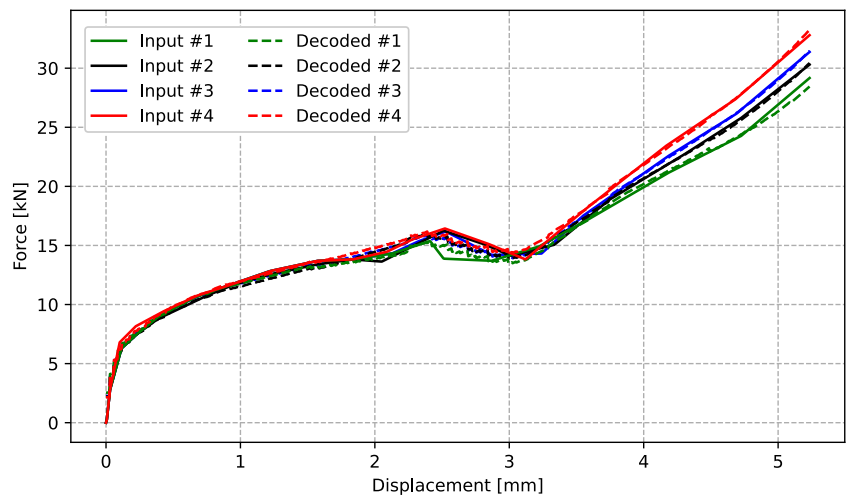
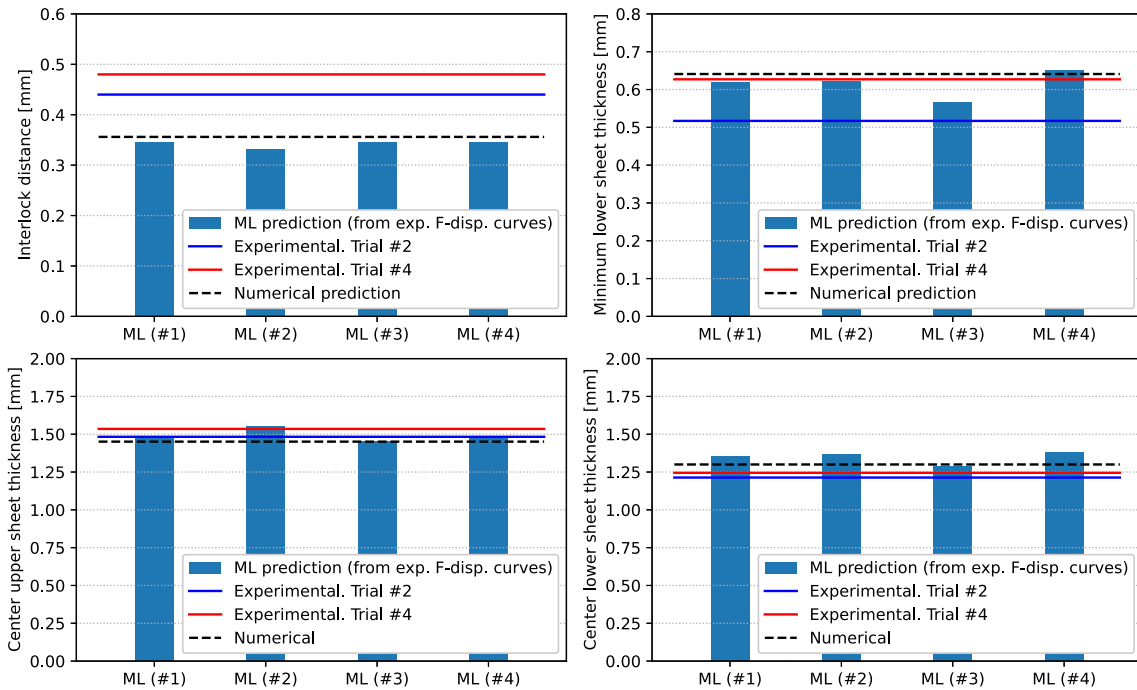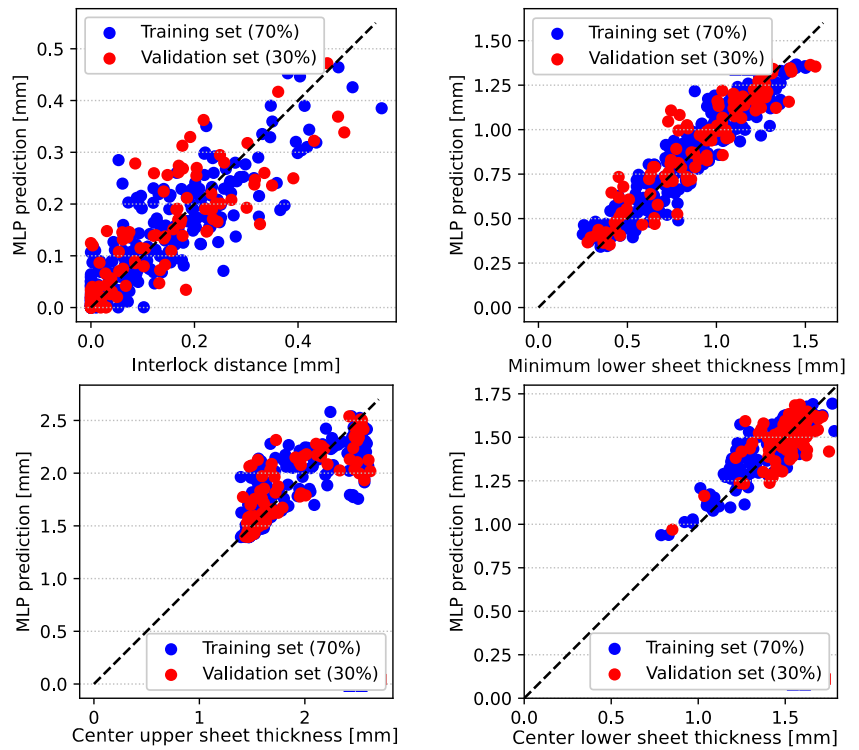**Fig. 11** Numerical and ML-predicted cross-sectional features

Fig. 12 Predicted riveting cross-sectional features (from the experimental force-displacement curves)

with the geometrical parameters observed experimentally and the ones provided by the FE model. However, interlock has slightly been underpredicted with respect to the experimental observation (in line with the numerical data used for training, see Section 3).

6 Conclusions

This work proposes a ML scheme for the evaluation of key cross-sectional features of a SPR joint, based on the punch force-displacement curves obtained during the riveting process. This allows the later assessment of its quality and resistance without the need to evaluate some uncertain parameters, such as friction coefficients and material properties.

To achieve this goal, first an axisymmetric FE model for the simulation of the SPR process using ABAQUS software was presented, obtaining good agreement with the experimental data. Next, a parametric study was prepared by sampling the material properties and the friction coefficients based on the LHS design of experiments. The postprocessed results provided by this FE model, containing a set of force-displacement curves and their corresponding cross-sectional features, were used for training the ML model.

Then, the dimensionality reduction was performed to the set of force-displacement curves by employing a CAE in order to obtain their reduced-dimension latent space, while reducing possible noise present. Finally, the correlation of the data points in the reduced latent space with the output geometric parameters, is straightforward using a simple MLP.

Results showed that good accuracy was obtained for each of the four considered key geometric features (interlock distance, minimum thickness of the lower sheet, center thickness of the upper/lower sheets) for the simulated validation subset. However, accuracy of the method was slightly lower for the experimental force-displacement curves, due to the minor discrepancy between the experimental and simulated geometric results. The aim of the authors was to prove the validity of the method, and they propose to circumvent this problem by training the ML model only with experimental data.

Declarations

References

1. Abe Y, Kato T, Mori K (2006) Joinability of aluminium alloy and mild steel sheets by self piercing rivet. J Materials Process Technol 177(3):417–421

2. He X, Pearson I, Young K (2008) Self-pierce riveting for sheet materials: State of the art. J Materials Process Technol 199(3):27–36

3. Soomro IA, Pedapati SR, Awang M (2022) A review of advances in resistance spot welding of automotive sheet steels: emerging methods to improve joint mechanical performance. Int J Adv Manuf Technol 118:1335–1366

4. Qin DL, Chen C (2022) Failure behavior and mechanical properties of novel dieless clinched joints with different sheet thickness ratios. J Cent South Univ 29(9):3077–3087

5. Zhang X, Chen C (2022) Experimental investigation of joining aluminum alloy sheets by stepped mechanical clinching. J Mater Res Technol 19(7):566–577

6. Ren X, Chen C (2023) Research on mechanical clinching process for dissimilar aluminum alloy sheets with inclined surface. J Manuf Process 89:362–370

7. Ouyang X, Chen C (2023) Research on the joining of aluminum alloy and high-strength steel by dieless clinched-adhesive processes. J Mater Res Technol 24(5):5526–5540

8. Lennon R, Pedreschi R, Sinha BP (1999) Comparative study of some mechanical connections in cold formed steel. Constr Build Mater 13:109–116

9. Cai W, Wang PC, Yang W (2005) Assembly dimensional prediction for self-piercing riveted aluminum panels. Int J Machine Tools Manuf 45(3):695–704

10. Sun X, Stephens EV, Khaleel MA (2007) Fatigue behaviors of self-piercing rivets joining similar and dissimilar sheet metals. Int J Fatigue 29(3):370–386

11. He X (2010) Recent development in finite element analysis of clinched joints. Int J Adv Manuf Technol 48:607–612

12. Li B, Fatemi A (2006) An experimental investigation of deformation and fatigue behavior of coach peel riveted joints. Int J Fatigue 28(3):9–18

13. Atzeni E, Ippolito R, Settineri L (2009) Experimental and numerical appraisal of self-piercing riveting. CIRP Annals 58(3):17–20

14. Hoang NH, Hopperstad OS, Langseth M, Westermann I (2013) Failure of aluminium self-piercing rivets: An experimental and numerical study. Mater Design 49(3):323–335

15. Hönsch F, Domitner J, Sommitsch C, Götzinger B, Kölz M (2018) Numerical simulation and experimental validation of self-piercing riveting (spr) of 6xxx aluminium alloys for automotive applications. J Phys: Confer Series 1063:3

16. Ren X-Q, Chen C, Ran X-K, Li Y-X, Zhang X-G (2021) Microstructure evolution of aa5052 joint failure process and mechanical performance after reconditioning with tubular rivet. Trans Nonferrous Metals Soc China 31:3380–3393

17. Atzeni E, Ippolito R, Settineri L (2007) Fem modeling of self-piercing riveted joint. Key Eng Mater 344(3):655–662

18. Porcaro R, Hanssen AG, Langseth M, Aalberg A (2006) Self-piercing riveting process: An experimental and numerical investigation. J Mater Process Technol 171(3):10–20

19. Daoud M, Gomes R, Kohout N, Balan T (2021) Effect of material behavior on dissimilar metal self-piercing riveting parameters based on finite element modeling for automotive applications. SIA Simulation Numérique Conference Proceedings

20. Karathanasopoulos N, Pandya KS, Mohr D (2021) Self-piercing riveting process: Prediction of joint characteristics through finite element and neural network modeling. J Adv Join Process 3(3):100040

21. Karathanasopoulos N, Mohr D (2022) Strength and failure of self-piercing riveted aluminum and steel sheet joints: Multi-axial experiments and modeling. J Adv Join Process 5(3):100107

22. Casalino G, Rotondo A, Ludovico A (2008) On the numerical modelling of the multiphysics self piercing riveting process based on the finite element technique. Adv Eng Softw 39(3):787–795

23. Haykin SO (2010) Neural Networks and Learning Machines. Pearson Education, Limited, 3rd edition ed

24. Brunton SL, Kutz JN (2019) Data-Driven Science and Engineering. Cambridge University Press, 3

25. Zhao H, Han L, Liu Y, Liu X (2021) Quality prediction and rivet/die selection for spr joints with artificial neural network and genetic algorithm. J Manuf Process 66(3):574–594

26. Fang Y, Huang L, Zhan Z, Huang S, Liu X, Chen Q, Zhao H, Han W (2022) A framework for calibration of self-piercing riveting process simulation model. J Manuf Process 76(3):223–235

27. Jain V, Seung HS (2008) Natural image denoising with convolutional networks. Advances in Neural Information Processing Systems 21 (NIPS 2008)

28. Rumelhart DE, Hinton GE, Williams RJ (1988) Learning internal representations by error propagation. Readings Cogn Sci 3:399–421

29. Baldi P (2021) Deep Learning in Science. Cambridge University Press

30. Goodfellow IJ, Pouget-Abadie J, Mirza M, Xu B, Warde-Farley D, Ozair S, Courville A, Bengio Y (2014) Generative adversarial nets

31. Oh S, Kim HK, Jeong TE, Kam DH, Ki H (2020) Deep-learning-based predictive architectures for self-piercing riveting process. IEEE Access 8:116254–116267

32. Kim HK, Oh S, Cho KH, Kam DH, Ki H (2021) Deep-learning approach to the self-piercing riveting of various combinations of steel and aluminum sheets. IEEE Access 9:79316–79325

33. von Mises R (1928) Mechanik der plastischen formänderung von kristallen. ZAMM - Z Angew Math Mech 8(3):161–185

34. Mohr D, Marcadet SJ (2015) Micromechanically-motivated phenomenological hosford-coulomb model for predicting ductile fracture initiation at low stress triaxialities. Int J Solids Struct 67–68(3):40–55

35. Peng J, Zhou P, Wang Y, Dai Q, Knowles D, Mostafavi M (2021) Stress triaxiality and lode angle parameter characterization of flat metal specimen with inclined notch. Metals 11(2):1627

36. Kramer MA (1991) Nonlinear principal component analysis using autoassociative neural networks. AIChE J 37(3):233–243

37. He X, He Q, Chen J-S (2022) Deep autoencoders for physics-constrained data-driven nonlinear materials modeling. Comput Methods Appl Mech Eng 385:3

38. Goodfellow I, Bengio Y, Courville A (2016) Deep learning. MIT Press

39. McKay MD, Beckman RJ, Conover WJ (1979) A comparison of three methods for selecting values of input variables in the analysis of output from a computer code. Technometrics 21(3):239